Thermal Stabilization of Defect Charge States and Finite-Temperature Charge Transition Levels

Tobias Hainer, Ethan Berger, Esmée Berger, Olof Hildeberg, Paul Erhart, and Julia Wiktor*
Department of Physics, Chalmers University of Technology, SE-41296, Gothenburg, Sweden

Point defects introduce localized electronic states that critically affect carrier trapping, recombination, and transport in functional materials. The associated charge transition levels (CTLs) can depend on temperature, requiring accurate treatment of vibrational and electronic free-energy contributions. In this work, we use machine-learned interatomic potentials to efficiently compute temperature-dependent CTLs for vacancies in MgO, LiF, and $CsSnBr_3$. Using thermodynamic integration, we quantify free-energy differences between charge states and calculate the vibrational entropy contributions at finite temperatures. We find that CTLs shift with temperature in MgO, LiF and $CsSnBr_3$ from both entropy and electronic contributions. Notably, in $CsSnBr_3$ a neutral charge state becomes thermodynamically stable above 60 K, introducing a temperature-dependent Fermi-level window absent at 0 K. We show that the widely used static, zero-kelvin defect formalism can miss both quantitative CTL shifts and the qualitative emergence of new stable charge states.

Defects play a crucial role in determining the physical properties of materials, influencing mechanical, electronic, and thermal behavior [1–5]. In particular, in functional applications such as photovoltaics they can both critically enhance and degrade the performance of solar energy devices [6–8]. Under realistic operating conditions, defects are unavoidable, making it essential to understand their impact on material behavior. In non-metals, charged defects can form and interact strongly with their environment through long-range Coulomb forces, influencing electronic and ionic processes. A key property of such defects is the charge transition level (CTL), which determines the thermodynamically favorable charge state for a given Fermi level. These CTLs are strongly influenced by the local chemical environment and therefore can be sensitive to temperature [9]. Accurate predictions of CTLs are essential for understanding defect-related properties, underscoring the need for detailed studies of their behavior including finite-temperature effects.

These defect-related properties have mainly been modeled using density functional theory (DFT), an accurate but computationally expensive method that becomes prohibitive for larger systems and/or is limiting when thermal effects are important. Many studies have mapped out CTLs at zero temperature for a wide range of materials [10–15]. While this allows a static characterization of defects, capturing behavior at finite temperatures remains a significant challenge. At finite temperatures, contributions from spin, electronic, vibrational and orientational entropy play a role in the free energy formulations [16, 17]. Among these, vibrational entropy typically has the largest impact and must be accounted for to accurately predict defect formation energies at finite temperatures. Incorporating this temperature dependence is therefore essential for reliable predictions above zero kelvin.

Finite-temperature effects have been explored within the (quasi-)harmonic approximation but also using molecular dynamics approaches [17–20], as well as through analyses of defect-induced volume changes and band-edge fluctuations [21]. These studies show that temperature induces only modest variations in defect formation free energies. However, a comprehensive understanding of the temperature dependence of CTLs is still emerging.

Here, we introduce a general finite-temperature framework for defect CTLs by combining DFT-trained neuroevolution potential (NEP) models with thermodynamic integration (TI) to quantify the temperature dependence of CTLs, as well as to determine the temperature dependence of optical transitions associated with vacancies in MgO, LiF, and $CsSnBr_3$. Building on the recent work on defect line shapes [19], for each material, a NEP model was trained on DFT reference data encompassing defect configurations across the relevant charge states. To explicitly represent the vacancy, the atoms neighboring the defect site were decorated with alternative atomic labels, enabling the potential to distinguish local environments associated with different charge states [19]. Two distinct TI paths were employed to accurately capture the temperature-induced changes in the CTLs: the Frenkel–Ladd path [22] and a direct integration path connecting machine-learned potentials (MLIPs) representing different charge states. Compared to previous finite temperature studies of defect free energies and CTLs, our work provides a practical and general workflow for obtaining finite temperature CTLs based on MLIPs, decomposes vibrational and band-edge (valence band maximum (VBM)) contributions across three representative material classes, and demonstrates the finite temperature emergence of a neutral defect charge state in $CsSnBr_3$ that is unstable at 0 K.

The defect formation free energy for a defect X in

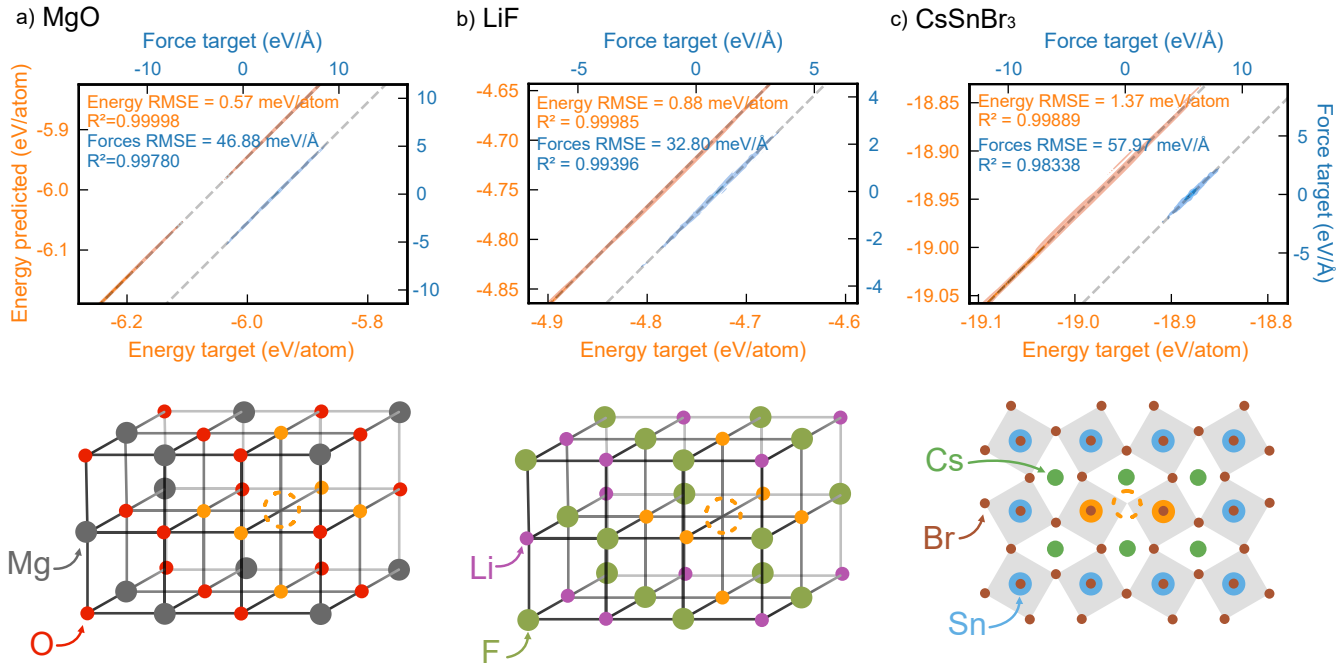

FIG. 1. **Machine-learned interatomic potential and illustrations of marked structures.** (a) The MgO model performance. Six closest Mg atoms to the oxygen vacancy are marked. (b) The LiF model performance. Six closest Li atoms to the fluorine vacancy are marked. (c) The $CsSnBr_3$ model performance. Two closest Sn atoms to the bromine vacancy are marked.

charge state q is given by Eq. (1).

$$G^f[X^q](T,\mu_e) = G_{\rm tot}[X^q](T) - G_{\rm tot}[{\rm bulk}](T) - \sum_i n_i\mu_i + q\left(E_{\rm VBM}(T)+\mu_e\right) + E_{\rm corr}(q). \quad (1)$$

Here, $G_{\rm tot}[X^q]$ and $G_{\rm tot}[{\rm bulk}]$ denote the Gibbs free energies of the defect-containing and pristine supercells, respectively. The term $\sum_i n_i\mu_i$ accounts for the chemical potential contributions associated with adding or removing atoms of type i. Since the CTL does not depend on the chemical potentials, all μ_i are treated as constants throughout this study. The term $q(E_{\rm VBM}+\mu_e)$ represents the energy required to add or remove q electrons referenced to the VBM. The temperature dependence of the VBM was obtained from molecular dynamics (MD) snapshots via deep core level alignment, with further details given in the SI (Sec. 1.3). $E_{\rm corr}$ is the correction term for finite-size effects, which in the present work is charge dependent and evaluated using the Freysoldt, Neugebauer and Van de Walle (FNV) correction scheme [23, 24]. The values for ionic chemical potentials, temperature dependent VBM shifts, and FNV corrections are reported in the SI (Sec. 1.3).

CTLs determine the thermodynamically favorable charge state of a defect at a given Fermi level. The CTL between charge states q and q', denoted as $\epsilon_{q/q'}$, is calculated from the difference in the defect formation free energies,

$$\epsilon_{q/q'} = \frac{G^f[X^q;\mu_e=0] - G^f[X^{q'};\mu_e=0]}{q'-q}. \quad (2)$$

To obtain well-converged TI results, we require an efficient way to perform MD simulations. To this end, NEP models were trained for MgO, LiF, and $CsSnBr_3$. For MgO and LiF, the reference data were generated using the PBEsol exchange–correlation functional [25], whereas for $CsSnBr_3$ the r2SCAN functional [26] was employed. The training dataset comprised both pristine and defective structures. For MgO, we included O vacancies with charge states 0 and +2; for LiF, F vacancies with charge states −1, 0, and +1; and for $CsSnBr_3$, Br vacancies with charge states −1, 0, and +1. In all training configurations, atoms neighboring a vacancy were labeled according to the charge state of that vacancy [19]. For MgO and LiF, the six Mg or Li atoms surrounding an O or F vacancy, respectively, were labeled, as illustrated in Fig. 1. In $CsSnBr_3$, the two Sn atoms closest to the defect were labeled. These labels encode the charge state of the associated vacancy.

To obtain free energy differences between charge states, including anharmonic contributions, we performed TI directly between charge states and validated against Frenkel–Ladd TI.

The direct path between charge states was implemented by duplicating the MLIP and relabeling the

atoms marked to represent a specific charge state. This produces two otherwise identical models that differ only in the assigned charge-state labeling of the defect environment. We then perform TI along a path between these two potentials, allowing us to compute the free-energy difference directly between the charge states. The resulting free energy difference provided the formation energy difference between the charge states, from which the CTLs were obtained.

The Frenkel–Ladd path [22], which connects the system described by the NEP model to a reference Einstein crystal with analytically known free energy, was used to calculate the free energy of both a pristine and defect cell. The formation energy was then obtained from Eq. (1). This approach yielded the absolute free energy of each structure at the target temperature, enabling accurate determination of defect formation free energies. These formation energies for different charge states were subsequently used in Eq. (2) to calculate the CTLs.

The performance of the NEP models is shown in Fig. 1. All models achieve R^2 scores close to 1 and low root mean square error (RMSE) scores.

Using TI with our MLIP, we obtained the Gibbs free energy of the charge states and pristine cells by integrating along the Frenkel-Ladd path. The defect formation energies were then evaluated using Eq. (1), including the VBM and correction terms.

These calculations enabled the construction of defect formation energy diagrams as a function of Fermi energy at various temperatures, as shown in Fig. 2a–c. In these plots, only the thermodynamically most stable charge state is shown at each Fermi energy. The positions of the VBM and CBM are marked by solid vertical lines, with colors corresponding to their respective temperatures. The shifts of both VBM and CBM are reported in the SI (Sec. 1.3). While we train our NEP models on data generated with semilocal functionals, we adjust the band edges in the formation energy plots for a more direct comparison with experimental data. It has been shown that CTLs of localized defects are found at similar absolute energies at different levels of theory [27]. Therefore, we only adjust the positions of the VBM and CBM in the plots. The shifts are taken from comparisons between calculations performed at the PBEsol level of theory for MgO and LiF, and at the r2SCAN level for $CsSnBr_3$, against hybrid-functional calculations using the PBE0(α) functional. In the case of $CsSnBr_3$, we additionally incorporate the shifts from including the spin-orbit coupling. For MgO and LiF, the values of the exact-exchange fraction ($\alpha = 0.34$ and $\alpha = 0.50$, respectively) are taken from Ref. [28], where they were determined using Koopmans' theorem applied to the hydrogen probe and the $H^+/0$ level. For $CsSnBr_3$ we use $\alpha = 0.26$, following Ref. 29, where the bromine vacancy was used as a probe.

From the formation energy diagrams, the CTLs at the temperatures where TI was performed were extracted, shown as the $\times$-markers in Fig. 2d–f. Note that the shifts of CTLs in these plots are reported relative to the temperature dependent VBM. Because the Frenkel–Ladd path requires extensive sampling to achieve convergence, the full temperature dependence of the CTLs was obtained using the direct TI path between charge states, also shown in Fig. 2d–f. The two TI approaches yield closely agreeing results at all temperatures, while the direct path is substantially more computationally efficient. This enhanced efficiency is evident from the faster convergence shown in the SI (Fig. S7). This likely arises from the smaller energy differences along the TI path between charge states compared with those encountered along the Frenkel–Ladd path. Moreover, evaluating the free-energy difference between charge states via the Frenkel–Ladd route requires two separate TI calculations, one for each charge state. In contrast, the direct charge-state path requires only a single TI calculation to obtain the CTL. Thus, the direct path both halves the minimum number of required TI runs and converges substantially faster than the Frenkel–Ladd path.

Optical transition energies ($E_{\mathrm{opt}(q'/q)}$ for transition from q to q') were calculated both at zero kelvin, using configurational coordinate diagrams (Fig. 3a-c), and at finite temperatures, using MD simulations (Fig. 3d-f). These transitions are reported relative to the temperature dependent VBM and move similarly to the associated CTLs. This is in agreement with previous results showing that the optical transition levels fluctuate similarly to the CTL in $CsPbBr_3$ [18]. The configuration coordinate diagram represents the potential energy surface (PES) as the structure transforms between different defect geometries, where the energy differences between charge states at their minima correspond to emission or absorption processes. These diagrams were constructed by interpolating between the relaxed geometries of different charge states while the MLIP predicted the energy along the transformation path. These represent the zero-kelvin optical transitions, as they are derived from relaxed geometries. At finite temperatures starting at 10 K, MD trajectories of defect-containing cells were generated in charge state q, while the energies were simultaneously evaluated for charge state q'. The energy differences between these states correspond to the optical transition energies between states q and q', reflecting electronic excitations or absorption occurring on timescales too short for atomic relaxation. The temperature-dependent optical transition levels are shown in Fig. 3d-f. The shaded regions represent the widths of the sampled emission and absorption distributions. For each temperature, the mean values and distribution widths were extracted from individual NPT ensemble simulation runs with durations ranging from 0.2 ns to 5 ns.

Oxygen vacancies in MgO with charge states +2 and 0 were investigated, resulting in one CTL. This CTL exhibits a clear temperature dependence (Fig. 2a, d) that is

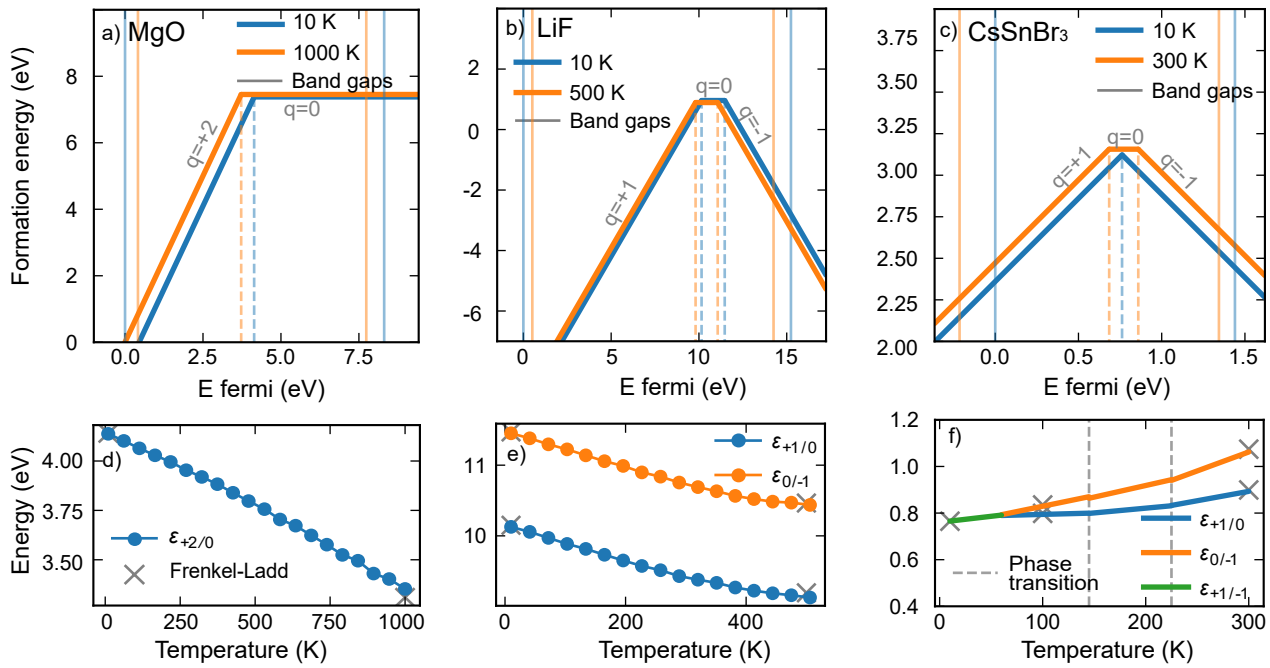

FIG. 2. **Temperature-dependent CTLs** for MgO, LiF, and $CsSnBr_3$ with regard to VBM position. Dashed lines represent the positions of the CTLs and solid vertical lines indicate VBM and CBM positions, colored according to the temperature they represent. (a,d) The $\varepsilon_{+2/0}$ level in MgO shifts by approximately $-785\,\text{meV}$ over a temperature range of 1000 K. (b,e) In LiF, the $\varepsilon_{+1/0}$ and $\varepsilon_{0/-1}$ levels shift by about $-994\,\text{meV}$ and $-1035\,\text{meV}$, respectively, over 500 K. (c,f) The CTLs exhibited a shift of roughly 111 meV, 324 meV and 218 meV over the 300 K for the transitions between $+1/0$, $0/-1$ and $+1/-1$ respectively. Notably, a region where the neutral charge state is thermodynamically favorable is introduced around 60 K.

driven by both vibrational entropy and a shift in VBM. The direct path between charge states yielded a CTL shift of $-0.785\,\text{meV K}^{-1}$.

Over the temperature range studied, the VBM increases by approximately 414 meV, see Fig. S9 for details. This shift contributes to roughly half of the CTL movement. Excluding this shift from the total free energy change, the vibrational contribution from the path between different charge states averages $-0.371\,\text{meV K}^{-1}$.

For MgO, the optical transitions between the neutral and +2 charge states were considered. From the configurational coordinate diagram (Fig. 3a) these transitions appear as the energy difference between the states in the their respectively relaxed geometries. We note that these zero kelvin vertical transitions are in reasonably good agreement with previous work done within the G_0W_0 approximation and the Bethe-Salpeter approach [30]. Furthermore, the temperature dependence of these optical transitions and their fluctuation (Fig. 3d) reveals a decrease in transition energies, which aligns well with the observed change in the CTL. In this figure, the shaded area indicates the standard deviation of the sampled optical transition energies, showing that these distributions widen with increased temperature. This increase in distribution width is similar for both charge states.

For LiF, fluorine vacancies with charge state -1, 0 or $+1$ were investigated, leading to two CTLs as all states have a region of stability. Both CTLs exhibit a shift with temperature (Fig. 2b, e). The shifts in CTLs from the direct integration are $-1.988\,\text{meV K}^{-1}$ and $-2.070\,\text{meV K}^{-1}$ for the $+1/0$ and $0/-1$ transitions, respectively.

The shift in VBM over 500 K was around 605 meV (see Fig. S11). Excluding this from the CTLs movement, the shifts become $-0.778\,\text{meV K}^{-1}$ and $-0.860\,\text{meV K}^{-1}$ for the $+1/0$ and $0/-1$ transitions, respectively. This is a substantial shift, even when excluding the VBM contribution, underscoring the importance of including vibrational entropy.

For LiF, the optical transitions between the neutral and $+1/-1$ charge states were considered (Fig. 3b, e). As in the case of MgO, the temperature dependence of these optical transitions and their fluctuations (Fig. 3e) show a slight decrease in transition energies with increasing temperature, which aligns well with the observed change in the CTL. Furthermore, the distribution widths of different transitions are on the same scale.

For $CsSnBr_3$, bromine vacancies with charge state -1, 0 or $+1$ were investigated. In both the orthorhombic and tetragonal phases there are non-degenerate vacancy sites. The difference in CTL positions between these are about 0.025 eV at zero kelvin and they all converge to the same values in the cubic phase as they become degenerate. In this section, we report findings from the defect site

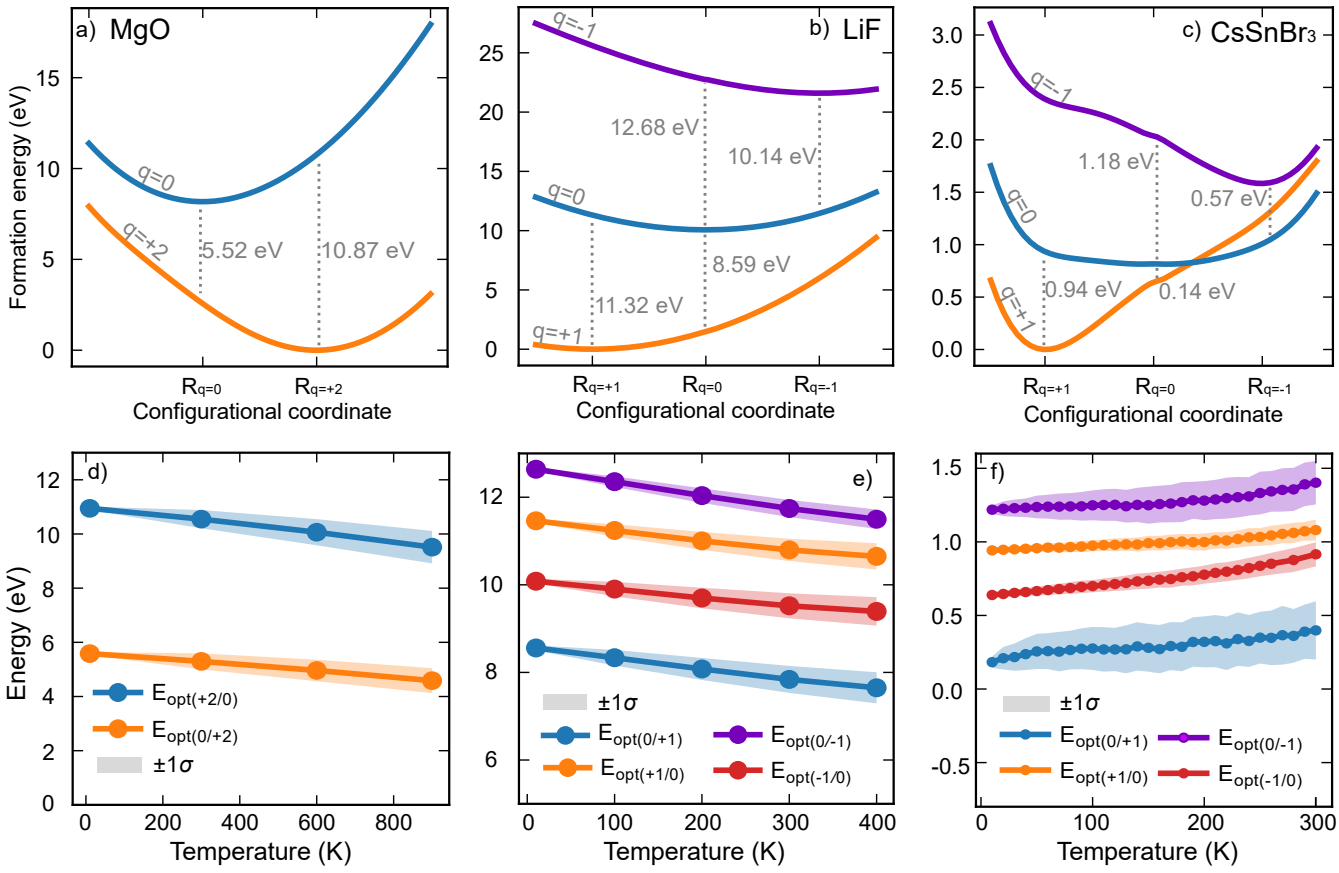

FIG. 3. **Configurational coordinate diagrams and temperature-dependent optical transitions** for MgO, LiF, and $CsSnBr_3$. (a–c) The energy difference at the relaxed geometry of each charge state defines the corresponding emission or absorption energy. The specific emission and absorption energies are shown as insets in the figures. (d–f) Emission and absorption energies during MD simulations at different temperatures. The shaded area represents the standard deviations of the sampled emission and absorption distributions.

that yields the lowest formation energy in the zero kelvin limit. At absolute zero, only the negative and positive charge states are thermodynamically stable. However, at temperatures above approximately 60 K, a region in which the neutral charge state becomes thermodynamically favored emerges (Fig. 2c). Due to the soft dynamics of this material, independent TI simulations fluctuated a lot in comparison to both LiF and MgO, requiring more sampling to reach convergence. For this reason, linear fits of the movement of the CTLs were performed. Additionally, two phase transitions are observed across the temperature range considered, an orthorhombic to tetragonal transition at 140 K and a tetragonal to cubic transition at 225 K. The linear fits were performed for each phase, showing minor changes in CTL slope at these transitions (Fig. 2f). Thus, structural phase transitions do not introduce discontinuous CTL shifts for this defect. The CTLs exhibited shifts of $0.370\,\mathrm{meV\,K^{-1}}$, $1.080\,\mathrm{meV\,K^{-1}}$, and $0.727\,\mathrm{meV\,K^{-1}}$ for the transitions between $+1/0$, $0/-1$, and $+1/-1$, respectively.

The VBM shift (−214 meV between 0 and 300 K, see Fig. S13) accounts for a substantial part of the CTL motion, but the sign and magnitude of the residual vibrational contribution differ between transitions, leading to the stabilization of the neutral state. Excluding the VBM shift, the CTL moves by $-0.343\,\mathrm{meV\,K^{-1}}$, $0.367\,\mathrm{meV\,K^{-1}}$, and $0.014\,\mathrm{meV\,K^{-1}}$ for the transitions between $+1/0$, $0/-1$, and $+1/-1$, respectively. This highlights that the vibrational entropy is the effect stabilizing the neutral charge state at higher temperatures in $CsSnBr_3$. These results show that, for $CsSnBr_3$, the CTL moves slightly and has a substantial contribution from the change in the VBM. This small movement in the CTLs due to vibrational entropy over this temperature range aligns well with previous results for halide perovskites [20]. However, the results also show the importance of including finite temperature effects as the neutral charge state emerges as thermodynamically stable for some Fermi energies only above 60 K.

For $CsSnBr_3$, the optical transitions between the neu-

tral and $+1/-1$ charge states were considered (Fig. 3c). The optical transitions and their fluctuations (Fig. 3f) exhibit an increase in transition energies. This is consistent with the CTLs of $CsSnBr_3$ and also with previous studies showing that the optical transitions shifts together with CTLs in $CsPbBr_3$ [18]. Furthermore, the vertical energy distributions associated with transitions from the neutral to the charged states are substantially broader than for all other transitions. This is reflected by the flat energy landscape of the neutral charge state in comparison with both the negative and positive charge state (Fig. 3c). When calculating absorption or emission events from the neutral charge state during MD, the system naturally exhibits larger structural fluctuations, as the flat energy landscape allows it to move in and out of geometries corresponding to the energy minima of the negative and positive charge states.

The temperature dependence of the CTLs across the investigated materials reveals distinct trends governed by the combination of vibrational entropy and VBM shifts.

For all materials investigated, substantial shifts in CTLs were identified. In MgO, the CTL movement is due to a near-equal shift in VBM and vibrational entropy. For LiF, contributions from vibrational entropy alone accounts for significant movements in CTL positions, which gets amplified when including the VBM movement. This emphasizes that lattice vibrations can drive significant CTL shifts and shows that these effects are of importance when modeling defect energetics. For $CsSnBr_3$, the temperature-induced movements of the CTLs are moderate and influenced mainly by VBM shifts. Effects such as these have been measured experimentally, for instance in GaSe where the difference between two CTLs, from Ga vacancies, increases from 0.17 eV to 0.38 eV over a range of 290.5 K [31]. This corresponds to a change of roughly $0.722\,\mathrm{meV\,K^{-1}}$, which is on the same order of magnitude as our results. Temperature shifts in the optical transition energies (Fig. 3d–f) have also been reported in previous experimental [32] and theoretical studies [19].

Furthermore, the most interesting observation related to the CTLs in $CsSnBr_3$ is the change that takes place at 60 K, where the neutral charge state becomes stable at some Fermi energies. The width of this stability range grows as temperature increases and at 300 K the neutral charge state is the most stable one across a substantial part of the band gap.

Our results highlight two points: The inclusion of finite-temperature effects is of importance due to the potential temperature dependence of CTLs and due to the possible introduction of new thermodynamically favorable charge states.

To conclude, we have quantified the temperature dependence of CTLs and optical transition energies for vacancies in MgO, LiF and $CsSnBr_3$ by employing MLIPs.

The direct TI path between charge states achieves high computational efficiency because the free energy differences along this path are small, in contrast to the much larger changes usually encountered in the Frenkel–Ladd path to an Einstein crystal. As a result, less sampling is required to obtain accurate estimates of the vibrational free-energy differences.

The results show that temperature can shift CTLs by hundreds of meV, with the cause of these shifts differing between materials. In MgO, LiF and $CsSnBr_3$ both vibrational and electronic (VBM) contributions are relevant to the movement of CTLs. Notably, in $CsSnBr_3$ we find the emergence of a thermodynamically stable neutral charge state only above 60 K. This shows that even if CTLs only vary slightly due to vibrational entropy contribution, this could have a significant impact by introducing entirely new thermodynamically stable charge states. Finite temperature shifts in CTLs and the emergence of new charge states as reported here are directly relevant for predicting doping limits and non-radiative recombination in wide-gap functional materials.

Together, these findings demonstrate that finite-temperature effects are essential for reliable predictions of defect energetics. We show that the widely used static formalism of defect modeling fails to capture details that are important under operating conditions for these materials.

DATA AVAILABILITY

All NEP models, as well as the DFT databases used to train these models, are available on Zenodo at `https://doi.org/10.5281/zenodo.17939378`

ACKNOWLEDGMENTS

We thank Sofia Cellini for useful comments. We acknowledge funding from the Swedish Strategic Research Foundation through a Future Research Leader programme (FFL21-0129), the Swedish Energy Agency (grant No. 45410-1), the Swedish Research Council (2018-06482, 2019-03993, and 2020-04935), the European Research Council (ERC Starting Grant No. 101162195), and the Knut and Alice Wallenberg Foundation (Nos. 2023.0032 and 2024.0042).The computations were enabled by resources provided by the National Academic Infrastructure for Supercomputing in Sweden (NAISS) at C3SE, PDC, and NSC, partially funded by the Swedish Research Council through grant agreement no. 2022-06725.

COMPETING INTERESTS

The authors declare that they have no competing interests.

* julia.wiktor@chalmers.se

[1] I. Lubomirsky, Mechanical properties and defect chemistry, Solid State Ionics **177**, 1639 (2006), solid State Ionics 15: Proceedings of the 15th International Conference on Solid State Ionics, Part I.

[2] S. T. Pantelides, The electronic structure of impurities and other point defects in semiconductors, Rev. Mod. Phys. **50**, 797 (1978).

[3] Y. V. Skrypnyk and V. M. Loktev, Electrical conductivity in graphene with point defects, Phys. Rev. B **82**, 085436 (2010).

[4] P. Gorai, T. Famprikis, B. Singh, V. Stevanović, and P. Canepa, Devil is in the defects: Electronic conductivity in solid electrolytes, Chemistry of Materials **33**, 7484 (2021).

[5] Z. Qu, T. D. Sparks, W. Pan, and D. R. Clarke, Thermal conductivity of the gadolinium calcium silicate apatites: Effect of different point defect types, Acta Materialia **59**, 3841 (2011).

[6] S. T. Pantelides, The electronic structure of impurities and other point defects in semiconductors, Reviews of Modern Physics **50**, 797 (1978).

[7] J. M. Ball and A. Petrozza, Defects in perovskite-halides and their effects in solar cells, Nature Energy **1**, 1 (2016).

[8] J. S. Park, S. Kim, Z. Xie, and A. Walsh, Point defect engineering in thin-film solar cells, Nature Reviews Materials **3**, 194 (2018).

[9] G. Greene-Diniz, K. J. Kuhn, P. K. Hurley, and J. C. Greer, First principles modeling of defects in the al2o3/in0.53ga0.47as system, Journal of Applied Physics **121**, 075703 (2017).

[10] D. Meggiolaro and F. De Angelis, First-principles modeling of defects in lead halide perovskites: Best practices and open issues, ACS Energy Letters **3**, 2206 (2018).

[11] M.-H. Du, Density functional calculations of native defects in ch3nh3pbi3: Effects of spin–orbit coupling and self-interaction error, The Journal of Physical Chemistry Letters **6**, 1461 (2015), pMID: 26263152.

[12] Y. Liang, X. Cui, F. Li, C. Stampfl, S. P. Ringer, and R. Zheng, First-principles investigation of intrinsic point defects in perovskite cssnbr$_3$, Phys. Rev. Mater. **5**, 035405 (2021).

[13] C. Linderälv, A. Lindman, and P. Erhart, A unifying perspective on oxygen vacancies in wide band gap oxides, The Journal of Physical Chemistry Letters **9**, 222 (2018).

[14] C. Freysoldt, B. Grabowski, T. Hickel, J. Neugebauer, G. Kresse, A. Janotti, and C. G. Van de Walle, First-principles calculations for point defects in solids, Rev. Mod. Phys. **86**, 253 (2014).

[15] A. Alkauskas, P. Broqvist, and A. Pasquarello, Defect levels through hybrid density functionals: Insights and applications, physica status solidi (b) **248**, 775 (2011).

[16] Y. Mishin, M. R. Sørensen, and A. F. Voter, Calculation of point-defect entropy in metals, Philosophical Magazine A **81**, 2591 (2001).

[17] I. Mosquera-Lois, S. R. Kavanagh, J. Klarbring, K. Tolborg, and A. Walsh, Imperfections are not 0 k: free energy of point defects in crystals, Chem. Soc. Rev. **52**, 5812 (2023).

[18] A. V. Cohen, D. A. Egger, A. M. Rappe, and L. Kronik, Breakdown of the Static Picture of Defect Energetics in Halide Perovskites: The Case of the Br Vacancy in CsPbBr3, The Journal of Physical Chemistry Letters **10**, 4490 (2019).

[19] C. Linderälv, N. Österbacka, J. Wiktor, and P. Erhart, Optical line shapes of color centers in solids from classical autocorrelation functions, npj Computational Materials **11**, 101 (2025).

[20] I. Mosquera-Lois and A. Walsh, Dynamic Vacancy Levels in $CsPbCl_3$ Obey Equilibrium Defect Thermodynamics, PRX Energy **4**, 043008 (2025).

[21] S. Qiao, Y.-N. Wu, X. Yan, B. Monserrat, S.-H. Wei, and B. Huang, Temperature effect on charge-state transition levels of defects in semiconductors, Phys. Rev. B **105**, 115201 (2022).

[22] R. K. R. Addula, S. K. Veesam, and S. N. P. and, Review of the frenkel–ladd technique for computing free energies of crystalline solids, Molecular Simulation **47**, 824 (2021).

[23] C. Freysoldt, J. Neugebauer, and C. G. Van de Walle, Fully ab initio finite-size corrections for charged-defect supercell calculations, Phys. Rev. Lett. **102**, 016402 (2009).

[24] C. Freysoldt, J. Neugebauer, and C. G. Van de Walle, Electrostatic interactions between charged defects in supercells, physica status solidi (b) **248**, 1067 (2011).

[25] J. P. Perdew, A. Ruzsinszky, G. I. Csonka, O. A. Vydrov, G. E. Scuseria, L. A. Constantin, X. Zhou, and K. Burke, Restoring the density-gradient expansion for exchange in solids and surfaces, Phys. Rev. Lett. **100**, 136406 (2008).

[26] J. W. Furness, A. D. Kaplan, J. Ning, J. P. Perdew, and J. Sun, Accurate and Numerically Efficient r^2 SCAN Meta-Generalized Gradient Approximation, The Journal of Physical Chemistry Letters **11**, 8208 (2020).

[27] W. Chen and A. Pasquarello, Correspondence of defect energy levels in hybrid density functional theory and many-body perturbation theory, Physical Review B—Condensed Matter and Materials Physics **88**, 115104 (2013).

[28] G. Miceli, W. Chen, I. Reshetnyak, and A. Pasquarello, Nonempirical hybrid functionals for band gaps and polaronic distortions in solids, Physical Review B **97**, 121112 (2018).

[29] T. Bischoff, J. Wiktor, W. Chen, and A. Pasquarello, Nonempirical hybrid functionals for band gaps of inorganic metal-halide perovskites, Physical Review Materials **3**, 123802 (2019).

[30] P. Rinke, A. Schleife, E. Kioupakis, A. Janotti, C. Rödl, F. Bechstedt, M. Scheffler, and C. G. Van de Walle, First-principles optical spectra for f centers in mgo, Phys. Rev. Lett. **108**, 126404 (2012).

[31] R. A. Redkin, N. I. Onishchenko, A. V. Kosobutsky, V. N. Brudnyi, X. Su, and S. Y. Sarkisov, Temperature-dependent optical absorption and dlts study of as-grown and electron-irradiated gase crystals, Crystals **15**, 10.3390/cryst15040372 (2025).

[32] K. B. Nam, J. Li, J. Y. Lin, and H. X. Jiang, Optical properties of aln and gan in elevated temperatures, Applied Physics Letters **85**, 3489 (2004).

Supporting Information

Thermal Stabilization of Defect Charge States and Finite-Temperature Charge Transition Levels

Tobias Hainer, Ethan Berger, Esmée Berger, Olof Hildeberg, Paul Erhart, and Julia Wiktor*
Department of Physics, Chalmers University of Technology, SE-41296, Gothenburg, Sweden
* julia.wiktor@chalmers.se

Contents

1 Supplementary Figures

1.1 Machine-learned potentials

Here, the losses during training are presented for all models as well as the parity plots showing the performance for energies, forces, virials, and stresses.

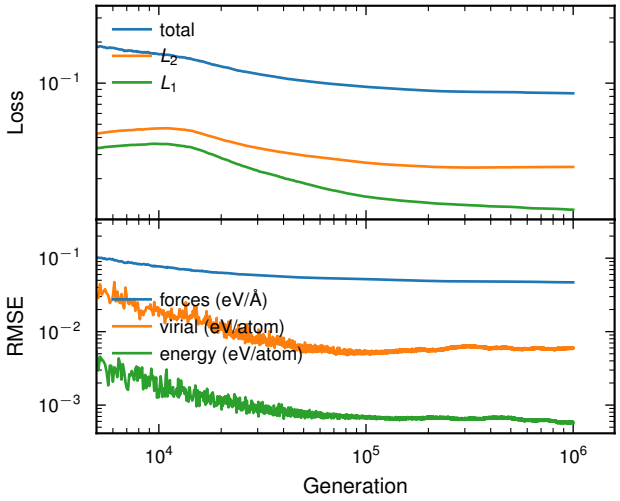

Fig. S1: Loss function during training of MLIP for MgO.

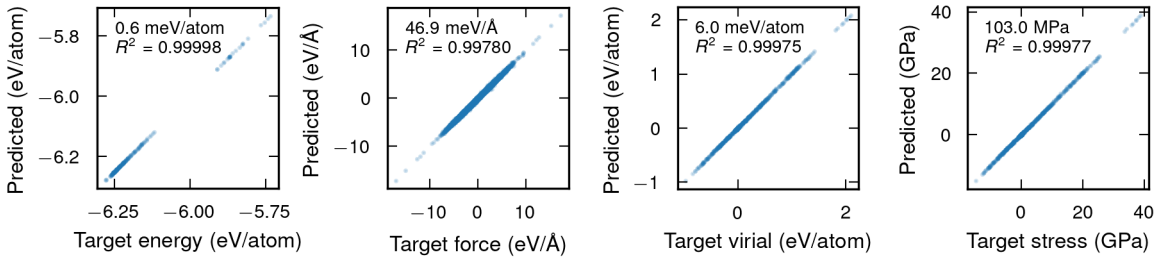

Fig. S2: Parity plot for energies, forces, virials and stresses in MgO.

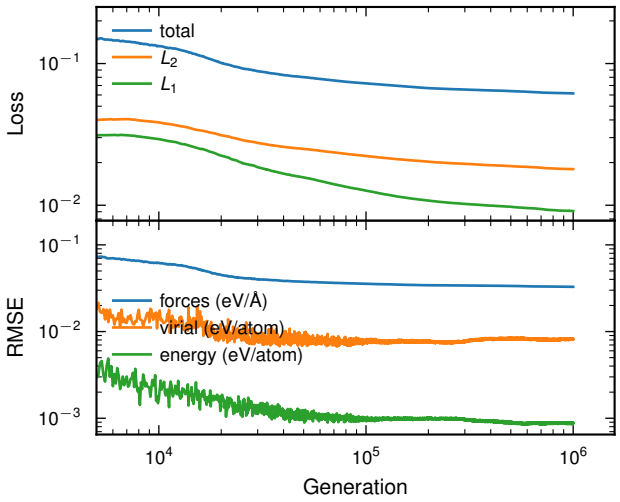

Fig. S3: Loss function during training of MLIP for LiF.

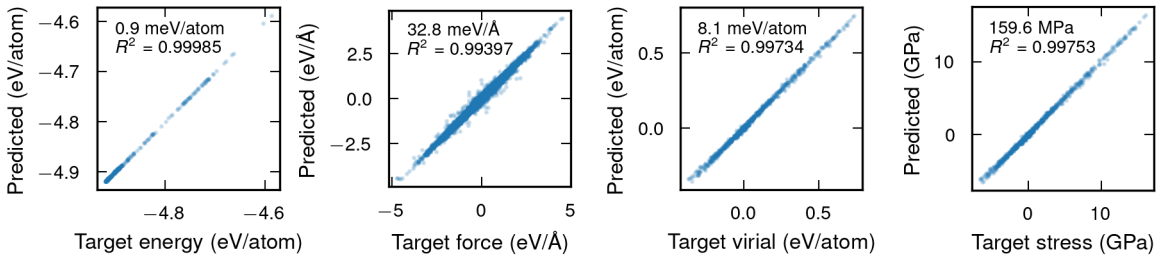

Fig. S4: Parity plot for energies, forces, virials and stresses in LiF.

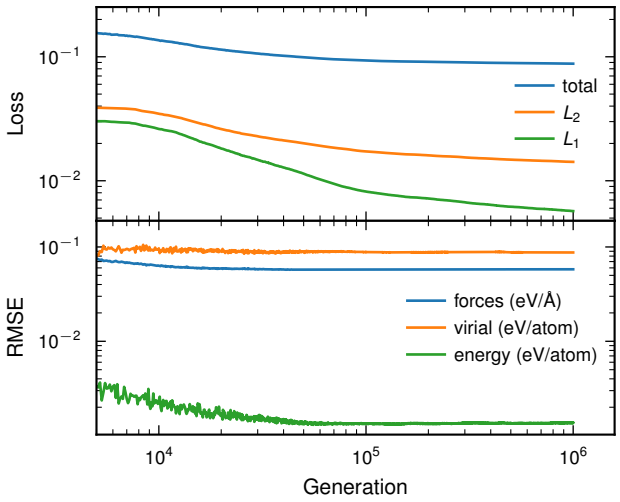

Fig. S5: Loss function during training of MLIP for $CsSnBr_3$.

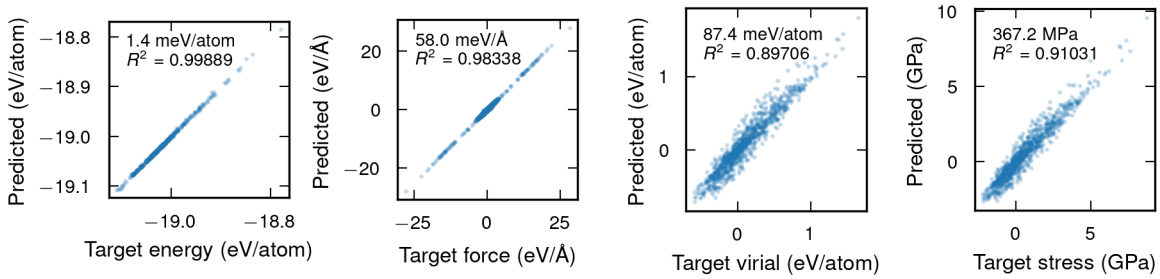

Fig. S6: Parity plot for energies, forces, virials and stresses in $CsSnBr_3$.

1.2 Comparison of thermodynamic integration paths

To illustrate the computational efficiency of the direct integration path, a benchmark of this method in comparison with the Frenkel-Ladd path was made for the free energy difference between the charge states 0 and +2 for an oxygen vacancy in MgO at 50 K. From Figure S7 it is clear that the direct path converges more quickly than the Frenkel-Ladd method, with its standard error for 3 runs outperforming the Frenkel-Ladd path for 30 runs for all numbers of steps. Note that the energies reported here are not corrected with regard to valence band maximum (VBM) and the FNV scheme, but instead are the raw data obtained from the methods.

Based on this benchmark, a minimum of 30 Frenkel-Ladd runs were performed for each temperature, each with at least 50 000 steps. For the direct integration, at least 50 000 steps were performed for each temperature. The timestep used throughout this work was 1 fs.

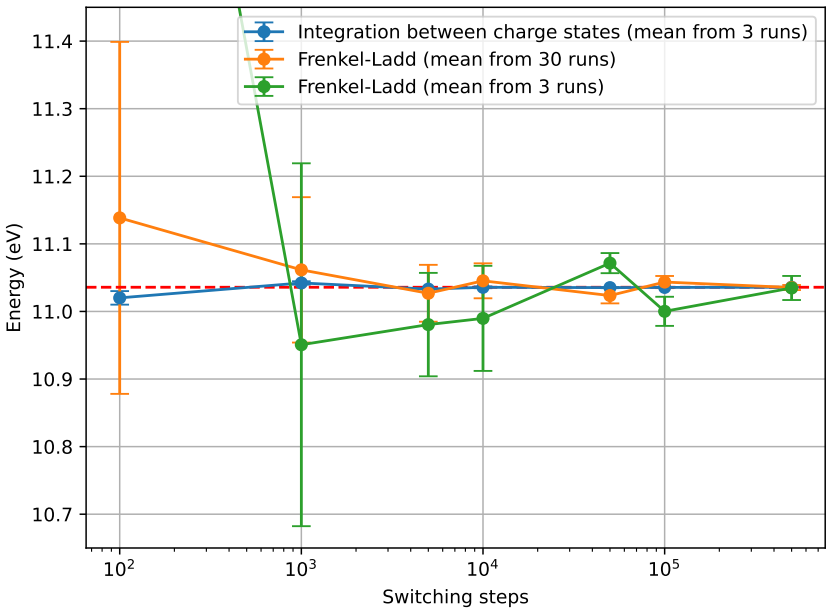

Fig. S7: Results and standard error for the energy difference between charge states 0 and +2 in MgO. Three cases were considered, direct integration between charge states averaged over 3 runs, and the Frenkel-Ladd path averaged over 3 and 30 runs. Convergence with number of steps is clearly much quicker for the direct integration method, as it essentially converges already after 1000 steps.

1.3 Chemical potential, corrections, and VBM shifts

Finite-size corrections for charged supercells were evaluated using the FNV scheme. All corrections were computed at 0 K and subsequently assumed to be temperature independent throughout this work.

The temperature dependence of the VBM was calculated using deep core states as reference levels. Snapshots from molecular dynamics (MD) simulations at finite temperatures were extracted, and density functional theory (DFT) calculations were performed to obtain the electronic DOS for each snapshot. A Gaussian fit was performed to deep levels for the electronic DOS of snapshots obtained from MD heating runs. The distance between the mean of this fit and the VBM was then calculated to track the VBM shift. This method is illustrated for one snapshot in Figure S8. The same method was used to track the conduction band maximum (CBM) movement.

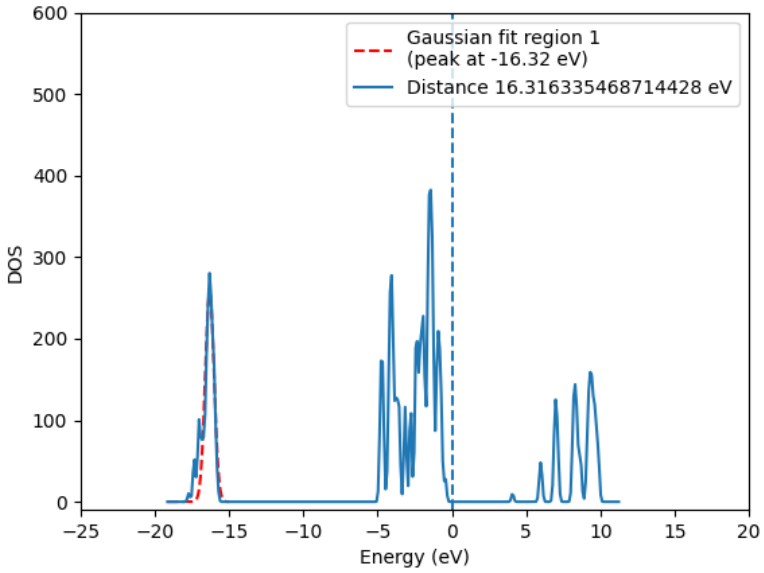

Fig. S8: Gaussian fits to DOS in MgODashed red curve is the gaussian fit to deep levels and dashed vertical line is the VBM position .

1.4 MgO

The ionic chemical potential of O was evaluated in a Mg-rich environment and found to be −4.45 eV. For MgO, the FNV scheme yields a correction of 722 meV for the +2 charge state. The VBM shift as a function of temperature and fit of this data can be seen in Figure S9. The CBM as a function of temperature can be seen in Figure S10

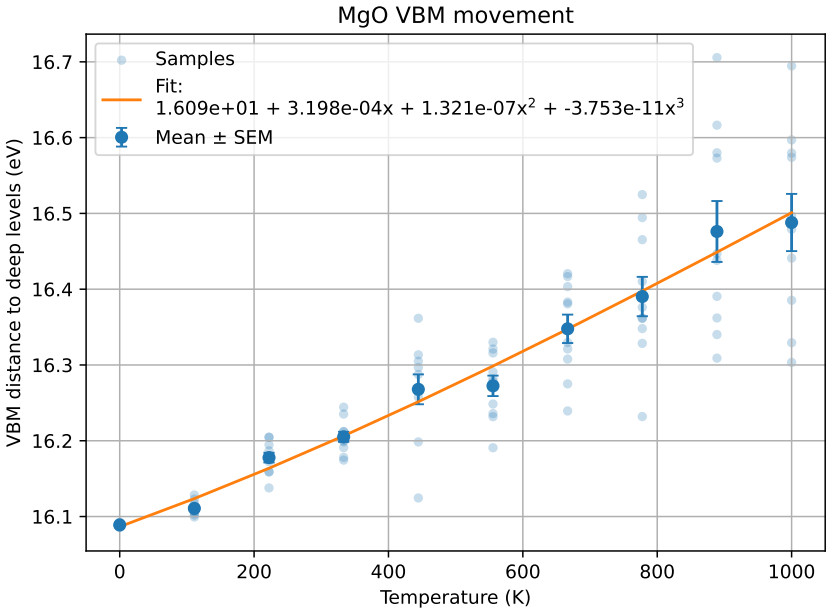

Fig. S9: VBM movement for MgO. A polynomial of degree 3 was fit to the data which is used in all calculations.

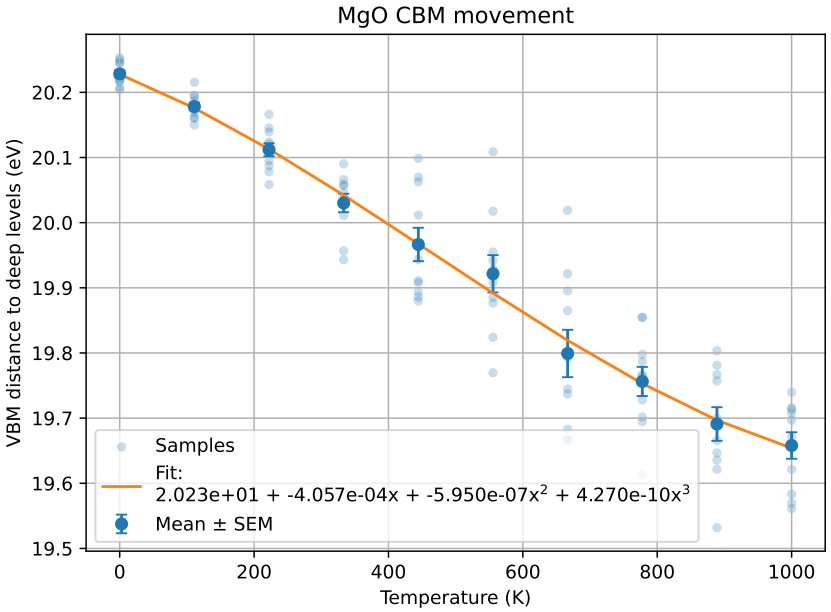

Fig. S10: CBM movement for MgO. A polynomial of degree 3 was fit to the data which is used in all calculations.

1.5 LiF

The ionic chemical potential of Li was evaluated in a Li-rich environment, and found to be −7.903 eV. For LiF, the calculated FNV corrections amount to 541 meV for the +1 charge state and 0.465 eV for the −1 charge state. The VBM shift as a function of temperature and fit of this data can be seen in Figure S11. The CBM as a function of temperature can be seen in Figure S12

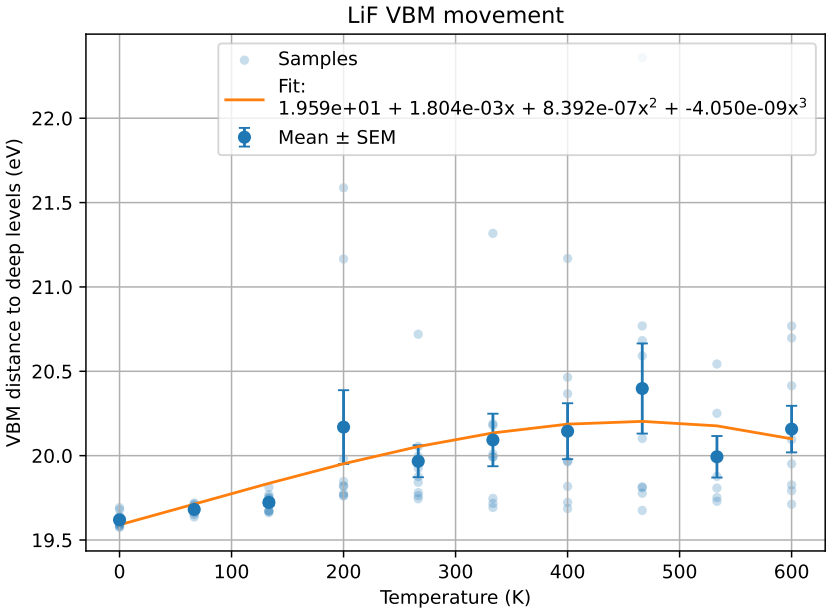

Fig. S11: VBM movement for LiF. A polynomial of degree 3 was fit to the data which is used in all calculations.

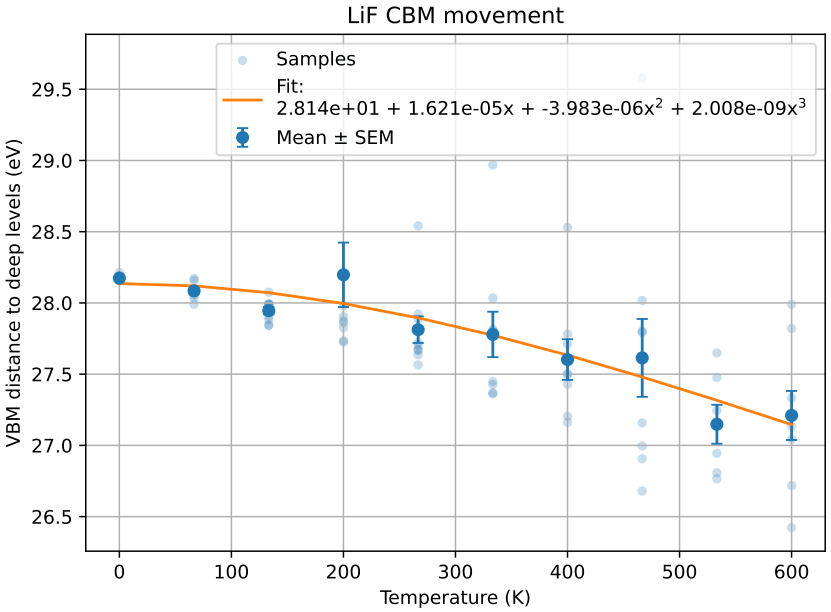

Fig. S12: CBM movement for LiF. A polynomial of degree 3 was fit to the data which is used in all calculations.

1.6 $CsSnBr_3$

The ionic chemical potential of Br was evaluated in a Br-rich environment and found to be −12.758 eV. In the case of $CsSnBr_3$, the +1 and −1 charge states require corrections of 172 meV and 113 meV, respectively. The VBM shift as a function of temperature and fit of this data can be seen in Figure S13. The CBM as a function of temperature can be seen in Figure S14

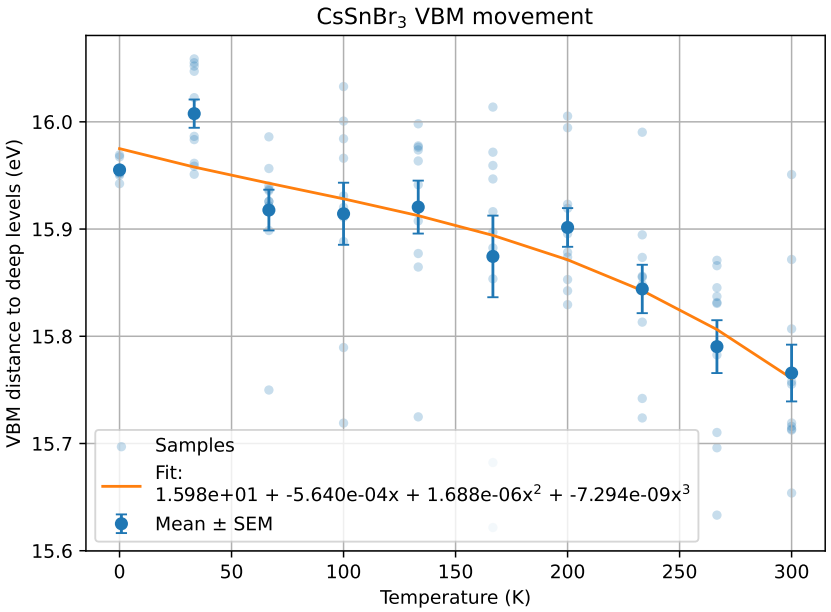

Fig. S13: VBM movement for $CsSnBr_3$. A polynomial of degree 3 was fit to the data which is used in all calculations.

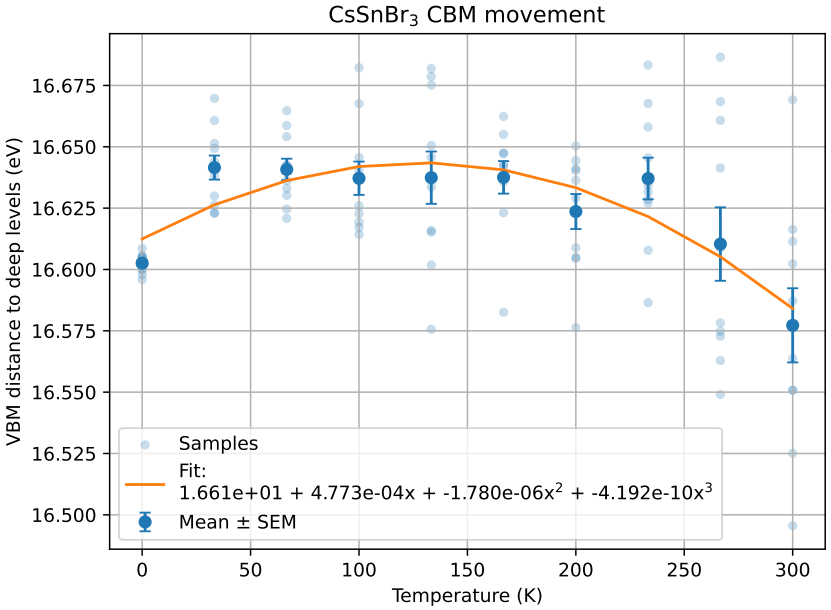

Fig. S14: CBM movement for $CsSnBr_3$. A polynomial of degree 3 was fit to the data which is used in all calculations.